Microscale Modeling of Fatigue Crack Growth at Particle Interfaces in Viscoelastic Asphalt Materials

Li'an Shen
College of Civil Engineering and Architecture
Zhejiang University
Hangzhou 310058, Zhejiang, China
Email: shenlian@zju.edu.cn

Juntao Wang
College of Civil Engineering and Architecture
Zhejiang University
Hangzhou 310058, Zhejiang, China
Email: gentlewang@zju.edu.cn

Chonghui Wang
College of Engineering and Physical Science
Aston University
B4 7ET, Birmingham, UK
Email: c.wang21@aston.ac.uk

Xue Luo, Ph.D
(corresponding author)
College of Civil Engineering and Architecture
Zhejiang University
Hangzhou 310058, Zhejiang, China
Email: xueluo@zju.edu.cn

Yuqing Zhang, Ph.D.
(corresponding author)
School of Transportation,
Southeast University,
Nanjing, 211189, China.
Email: zhangyuqing@seu.edu.cn

Abstract

The viscoelastic damage evolution at the microscale particle interfaces of asphalt mortar or mixtures fundamentally determines the material's fatigue crack growth and failure at the macroscale. However, existing microscale damage models are often based on empirical assumptions that depend on inter-particle stresses or forces, which are inaccurate or even incorrect for viscoelastic asphalt materials. In these materials, interfacial crack growth is governed by the viscoelastic energy release rate. To address the limitations of current models, a microscale viscoelastic fatigue damage model was developed using a pseudo J-integral-based Paris' law and implemented in a discrete element model of asphalt mortar using the PFC2D program. The viscoelastic constitutive behavior was represented by a generalized Maxwell model, and the relaxation moduli were determined through a uniaxial compressive dynamic modulus test. The Paris' law coefficients were calibrated by comparing model predictions with experimental results from indirect tensile fatigue tests of the material. The results show that the simulated fatigue life and crack area closely match laboratory test data, with an error margin within 15%. During the simulation of microscopic IDT fatigue damage, cracks hinder the horizontal transfer of forces within the cracked region, leading to stress concentrations in surrounding particles and a marked increase in their relative displacement. The connection of upper and lower cracks significantly reduces the specimen's load-bearing capacity. The variation in the number of contact breaks with fatigue load cycles is unaffected by the type of asphalt but is influenced by the applied stress level. These findings demonstrate that the pseudo J-integral-based Paris' law, when applied at particle interfaces, can effectively model crack growth at the microscale and accurately predict the fatigue damage performance of viscoelastic asphalt materials at the macroscale.

Keywords: Asphalt materials; Particle interfaces; Discrete element method (DEM); Fatigue crack; Indirect tensile test

1. Introduction

Fatigue cracking in asphalt pavement, caused by long-term vehicle loading cycles, significantly reduces the service life of pavement structures. Current fatigue testing of asphalt materials predominantly relies on laboratory experiments, including direct tensile tests, indirect tensile tests, three-point bending beam tests, and semi-circular bending tests. However, these macroscopic approaches have limitations; they assess the fatigue properties only at the macroscale and cannot effectively capture the complete process of damage and cracking at the microscale. To overcome these limitations, numerical simulation methods such as the finite element method (FEM) and the discrete element method (DEM) are used to study the micromechanical response of asphalt materials to fatigue damage. DEM enables cyclic tracking of the interfacial failure process between particles under fatigue loading at the mesoscopic scale, thereby providing a more realistic representation of fatigue damage accumulation. Furthermore, DEM demonstrates superior capability in addressing heterogeneous stress distributions within specimens subjected to localized loading conditions. Through explicit modeling of particle arrangement and the evolution of contact force chains, DEM offers direct visualization of material anisotropy. In contrast, FEM rooted in continuum mechanics assumptions, exhibits inherent limitations in capturing discontinuous behaviors such as particle detachment and microcrack propagation. Moreover, FEM is predominantly employed for macroscopic response prediction, where homogenized material properties are generally adopted. Since asphalt mixtures transition to a discontinuous state when damaged, DEM is advantageous for observing internal processes and microscale cracking.

The discrete element method (DEM), originally introduced by Cundall for rock mechanics analysis[1], has been extensively applied in pavement engineering since 1997. Chang et al.[2] enhanced the TRUBAL program by developing a hot mix asphalt model, which was validated through monotonic and cyclic testing. Subsequently, Collop et al.[3] created a DEM for asphalt mixtures to examine the effect of stress ratio on shear strain expansion rates using uniaxial and triaxial tests. Hyunwook Kim et al.[4] employed a cohesive zone model to simulate crack propagation in double cantilever beams, comparing initial stiffness and peak load between experimental and simulation results, yielding consistent findings. You et al.[5] developed a DEM-based simulation method for uniaxial compression tests of asphalt mixtures, establishing conversion relationships between macroscopic and microscopic parameters to model dynamic modulus and phase angle. Mahmoud et al.[6] utilized DEM to investigate the effects of aggregate gradation, shape characteristics, and strength on asphalt mixture cracking, recommending stronger aggregates due to higher stress levels observed in PFC mixtures. Liu et al.[7] studied the impact of discrete element size on creep stiffness, suggesting larger elements for simple tests to reduce simulation time, while smaller elements provide more accurate results for complex tests, such as permanent deformation and cracking. Ma et al.[8] simulated wheel tracking tests to predict rutting deformation in asphalt mixtures, offering a microscopic explanation of rut formation mechanisms. Chen et al.[9] explored the effects of compaction methods and frequencies on porosity distribution in asphalt mixtures, finding that gyratory compacted specimens exhibited more uniform air void distribution compared to vibratory compacted specimens. Gong et al.[10] investigated the influence of various combinations of coarse aggregate types on movement characteristics during rotary compaction of asphalt mixtures. Qian et al.[11] analyzed changes in aggregate positioning during compaction, noting that while compaction further reduces porosity, it has a limited effect on the distribution of large aggregates. Moreover, numerous scholars have employed DEM to simulate a range of tests on

asphalt mixtures, including uniaxial compression test[12-14], creep test[15-17], indirect tensile test[18-20], and shear strength test[21-23].

Recently, the DEM has been increasingly utilized by researchers to study the fatigue damage in pavement materials. Zhao et al.[24] employed a linear parallel bond model to develop a cement-stabilized gravel model and conducted semi-circular bending fatigue tests. During the loading process, the bonding radius in the linear parallel bond model was reduced using a radius multiplier, which increased both the normal and shear stresses between contact particles, improving the accuracy of fatigue damage simulation. Nguyen et al.[25], [26] introduced a novel fatigue bonding contact model for bonded materials, incorporating fatigue damage variables and evolution rules into a cohesive damage-plasticity framework, allowing for the accurate simulation of material responses under fatigue. Several studies have investigated fatigue in asphalt mixtures with viscoelastic properties. Li et al.[27] utilized PFC software to simulate the indirect tensile fatigue test of asphalt mixtures, analyzing fatigue crack propagation and internal force distribution at different stages, and comparing these results with laboratory experiments. Peng et al.[28], [29] developed a virtual asphalt mixture model using the Burgers model to investigate permanent deformation, shear stress, and transverse strain under traffic loads. By introducing a damage factor, they updated the elastic modulus E and viscosity η to reflect the material's evolving behavior. Ma et al.[30] established a virtual fatigue test of asphalt mixtures to assess the influence of porosity content, distribution, size, and orientation on fatigue life. Yang et al.[31] examined the distribution characteristics of contact force chains and micromechanical responses under fatigue loading through an asphalt mixture model and indirect tensile fatigue tests. Gao et al.[32] simulated the effects of stress distribution on specimen damage in Arcan Type I cracking tests by defining a critical stress threshold and applying a radius reduction method to model fatigue damage. Feng et al.[33] explored the failure mechanisms of asphalt mixtures during four-point bending tests by analyzing microscopic force chains.

The current fatigue damage models in the DEM for particle interfaces at the microscale are primarily designed for elastic cracking and are inadequate for predicting fatigue cracking in viscoelastic materials such as bitumen, mastic, and asphalt mixtures. In the case of asphalt mixtures, the fatigue damage formulas used by researchers have notable limitations. For instance, Ma et al.[30] and Peng et al.[28], [29] proposed fatigue damage functions derived from discrete element numerical simulations, as shown in Eq. (1-2). However, these damage evolution models are essentially empirical fits to time and force or stress data, lacking a solid mechanistic foundation or physical significance. The damage, represented by a reduction in the radius between particles, is based on phenomenological equations. Furthermore, the time variable in the equation refers to the simulation time, not the actual damage evolution time, which misrepresents the real damage progression and leads to inaccurate predictions of cracking at the microscale. Therefore, the empirical nature of the fatigue damage evolution model used in existing DEM modeling makes it unsuitable for varying loading modes and histories. Additionally, the Burgers viscoelastic model embedded in the PFC software lacks bonding functionality, preventing the simulation of viscoelastic tensile behavior.

$$D_t = D_0 - \int_0^t -m\left(1+\frac{t}{k}\right)^n e^{\beta\varphi_t/\varphi_n}dt \tag{1}$$

Where, D_0 is the original bonding diameter between the adjacent particles, D_t is the bonding diameter at loading time t under a fatigue loading, φ_t is the tensile force at loading time t, φ_n is the contacting tensile force at contacts, m, k, n and β are fatigue damage model parameters.

$$D(t) = 1 - \left(1 - t\lambda(1+n)\sigma_0^m\right)^{\frac{1}{1+n}} \tag{2}$$

Where, $D(t)$ is the material damage factor, σ_0 is the stress in the uniaxial stress state, λ, m, n are the material parameters relating to temperature.

For viscoelastic particulate materials such as asphalt mixtures, the rate of crack propagation is fundamentally determined by the cracking energy release rate, rather than by force or stress. Consequently, it is inappropriate to predict crack propagation speed using the ratio of force or stress to material strength, as is often done in the literature. Moreover, these empirical models fail to adequately account for how material parameters are determined, and the physical significance of these parameters remains unclear, resulting in non-unique fitting solutions. In this paper, the Burgers model is improved by integrating contact persistence and activation modules using the 'fish' programming language, addressing the issue of the model's lack of bonding functionality. Thus, the objective of this study is to develop a methodology that accurately represents the fatigue damage at particle interfaces (ball-ball) in DEM microscale simulations, enabling the modeling of fatigue damage in asphalt mixtures under dynamic cyclic loading. A J-integral-based Paris' law is applied to characterize viscoelastic fatigue damage in asphalt materials. The model parameters A and n are intrinsic material properties associated solely with the material's cracking resistance, and are independent of loading frequency or magnitude.

2. Discrete element modeling

2.1 Discrete element models for asphalt mortar

In PFC 5.0, two primary particle types, the ball and the clump, were employed to construct microscale models. A clump is composed of multiple pebbles that experience no relative deformation, and it is typically used to represent aggregate, while a ball is used to simulate asphalt. However, for computational efficiency in this study, aggregates smaller than 2.36 cm were considered part of the asphalt mortar, and a ball was used to model the mortar. In PFC2D, particles can be arranged uniformly in either cubic or hexagonal patterns, as shown in Fig. 1. Asphalt mortar was treated as a continuum, and thus a hexagonal uniform distribution was used to design the asphalt mortar specimens. This approach allowed for the generation of indirect tensile (IDT) asphalt mortar specimens through circular cutting, as illustrated in Fig. 2.

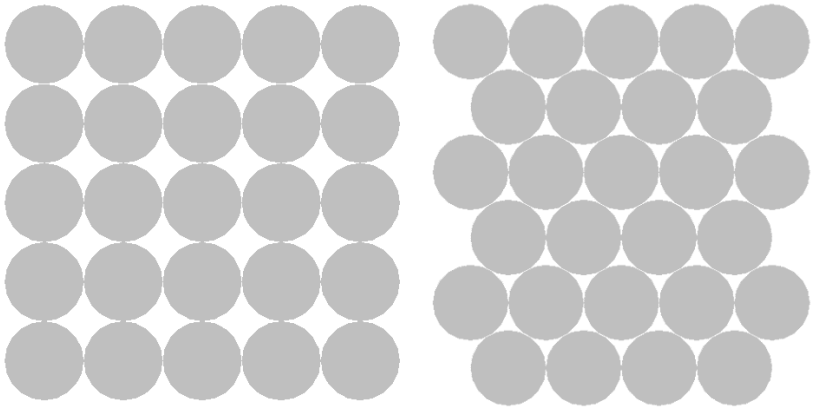

(a) Cubic shape (b) Hexagonal shape

Fig. 1. Arrangement of particles in discrete element models

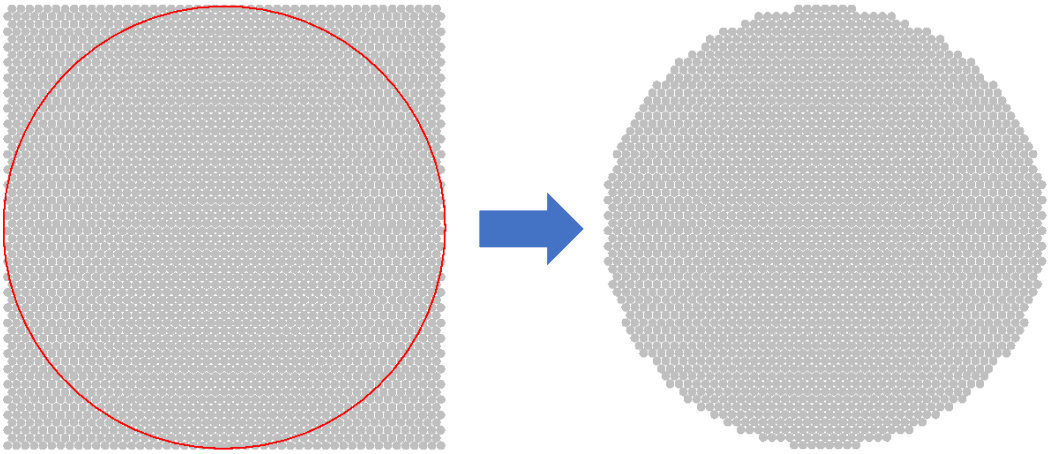

Fig. 2. The cutting way of asphalt mortar specimens

2.2 Improved Burgers model for viscoelastic contacts between particles

In the embedded contact model of PFC 5.0, the Burgers model is used to simulate the viscoelastic properties of asphalt mortar. However, the current Burgers model lacks a bonding function, limiting its applicability to compression-only scenarios between contact particles. Under tension, the contact bond breaks immediately, which fails to accurately capture the microscale damage behavior. To address this limitation, this paper proposes an enhancement to the embedded Burgers model by integrating a bonding function.

The Burgers model is composed of the Kelvin model and the Maxwell model in series in the normal and tangential directions. In the Maxwell model, there exists a series form of elastic modulus E_1 and viscosity η_1. In the Kelvin model, there exists a parallel form of elastic modulus E_2 and viscosity η_2. In the microscopic domain, the Burgers model exists in both the normal and tangential directions, as illustrated in Fig 3. Among them, k_{mn} is the Maxwell model normal stiffness, c_{mn} is the Maxwell model normal viscosity, k_{kn} is the Kelvin model normal stiffness, c_{kn} is the Kelvin model normal viscosity, k_{ms} is the Maxwell model shear stiffness, and c_{ms} is the Maxwell model shear viscosity. k_{ks} is the Kelvin model shear stiffness, c_{ks} is the Kelvin model shear viscosity. The conversion of Burgers model macro-parameters to micro-parameters is shown in Eq. (3-10).

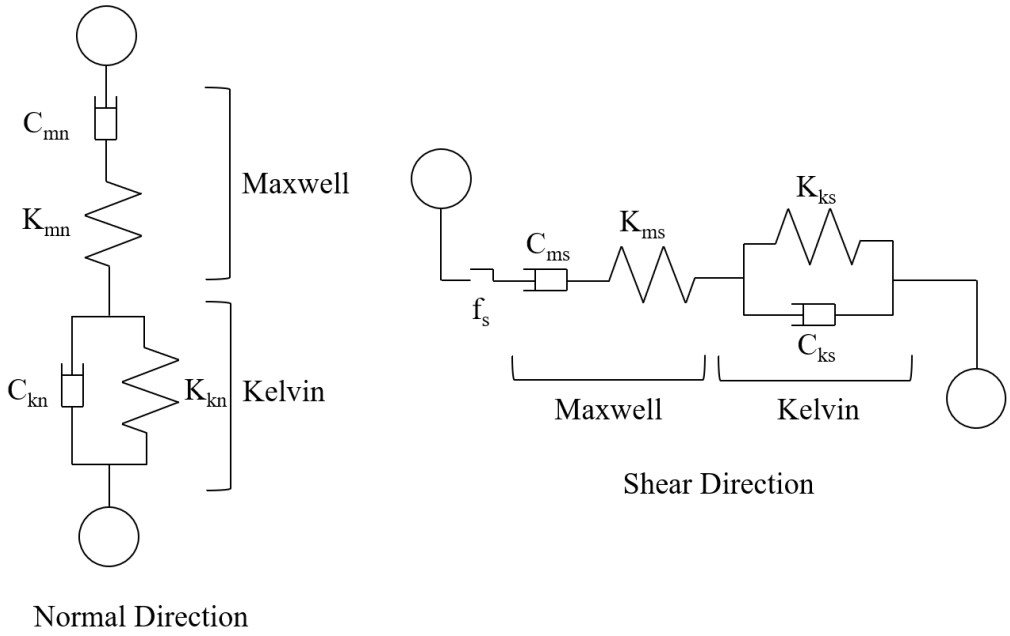

Fig. 3. Rheological components of Burgers model at DEM particle interfaces

$$k_{mn} = 2E_1 t \tag{3}$$

$$c_{mn} = 2\eta_1 t \tag{4}$$

$$k_{kn} = 2E_2 t \tag{5}$$

$$c_{kn} = 2\eta_2 t \tag{6}$$

$$k_{ms} = \frac{E_1}{1+\nu} t \tag{7}$$

$$c_{ms} = \frac{\eta_1}{1+\nu} t \tag{8}$$

$$k_{ks} = \frac{E_2}{1+\nu} t \tag{9}$$

$$c_{ks} = \frac{\eta_2}{1+\nu} t \tag{10}$$

Where, t is thickness, ν is Poisson's ratio.

The Burgers model was improved by implementing a bonding function. As illustrated in Fig 4, 'fish' scripting language was used to define the contact generation and breaking mechanisms. Firstly, the Burgers model contact key is set to be forcibly activated, and contact deletion is set to be disabled. This ensures that the Burgers model remains in contact under tensile stress, allowing it to exhibit viscoelastic properties. Additionally, the program includes a function to monitor contact forces within the Burgers model. The program calculates both the shear and normal tensile forces between contacts and compares them to their respective maximum values using a judgment function. If the contact shear force exceeds the maximum shear force or if the contact normal tension surpasses the maximum normal tension, the force persistence and activation functions are disabled, and the contact will be failure. This methodology enables the simulation and accurate characterization of the microscopic viscoelastic properties of asphalt materials.

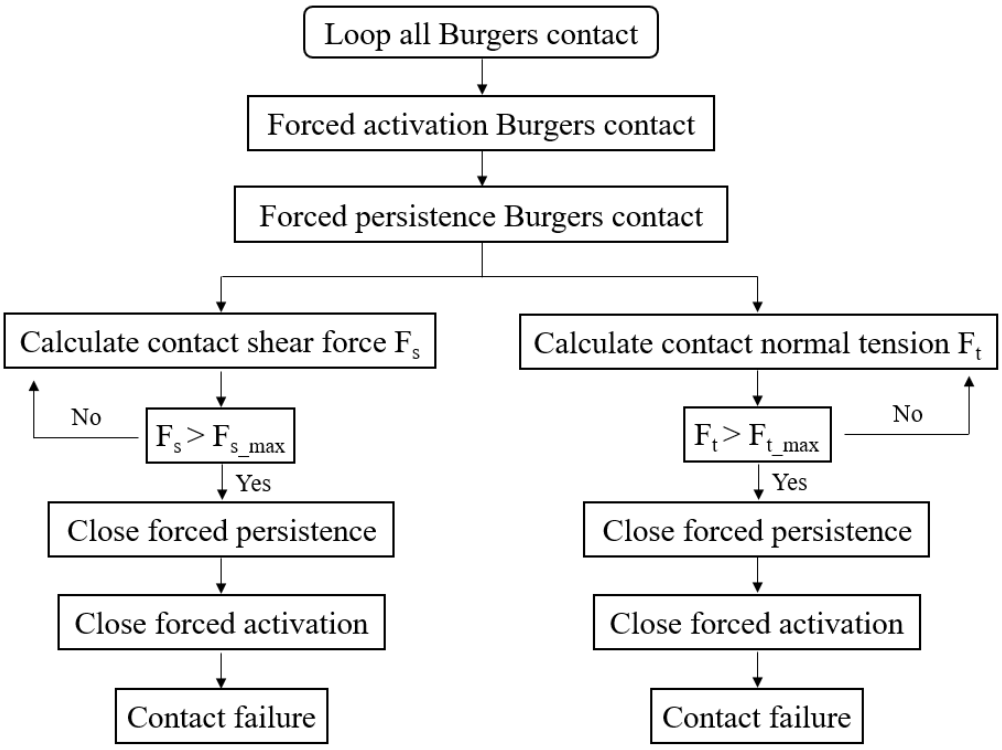

Fig. 4. Logical flow chart of improved Burgers model

2.3 J-integral based Paris' Law for fatigue damage evolution at the microscale

Fig. 5 illustrates the contact bond and crack form between ball-ball, assuming that the damage ξ is the ratio of the crack length a to the contact diameter d in the contact bond, as shown in Eq. (11).

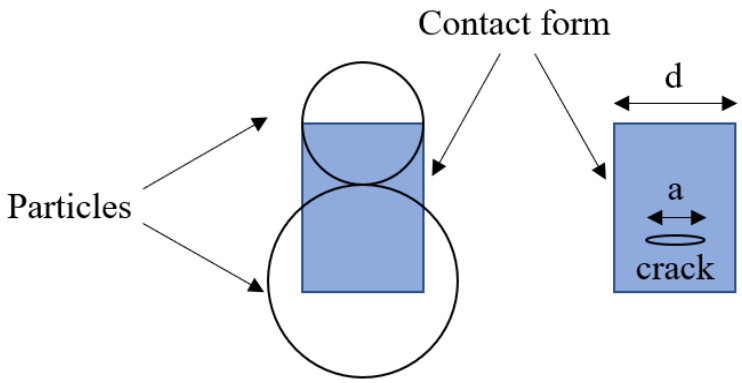

Fig. 5. Contact form and crack patterns between ball-ball

$$\xi = \frac{a}{d} \tag{11}$$

Where, a is crack length in the contact bond, d is contact diameter.

Therefore, in this paper, ΔJ integral is used to establish Paris's law for characterizing the viscoelastic fatigue damage process. As shown in Eq. (12).

$$\frac{d\xi}{dN} = \frac{A(\Delta J)^n}{d} \tag{12}$$

Where, A and n are material parameters. ΔJ is determined by Eq. (13)[34].

$$\Delta J = \frac{1-\nu^2}{E_R}\left(K_I^2 + K_{II}^2\right) + \frac{1+\nu}{E_R}K_{III}^2 \tag{13}$$

Where, E_R is representative elastic modulus, ν is the Poisson's ratio, K_I is the Mode I (opening) stress intensity factor; K_{II} is the Mode II (in-plane shear) stress intensity factor; and K_{III} is the Mode III (out of plane shear) stress intensity factor.

E_R is determined by Eq. (14)[34].

$$E_R = \frac{1}{2}\left[\left|E^*\right|_{f=\frac{1}{t_p}} + E\left(t=\frac{t_p}{2}\right)\right] \tag{14}$$

Where, $\left|E^*\right|$ is dynamic modulus, $E(t)$ relaxation modulus, f is load frequency, t_p is load pulse time.

For indirect tensile fatigue test of asphalt mortar, Type I and Type II cracking are generally considered. For Type I cracking (tension cracking), the stress intensity factor $\Delta K = K_I$. For Type II cracking (slip cracking), $\Delta K = K_{II}$ [35]. The expression is shown in Eq. (15-17).

$$\Delta K = \sqrt{\left(\Delta K_I\right)^2 + \left(\Delta K_{II}\right)^2} \tag{15}$$

$$\Delta K_I = Y_I\sqrt{\pi a}\left(\sigma_n^{\max} - \sigma_n^{\min}\right) \tag{16}$$

$$\Delta K_{II} = Y_{II}\sqrt{\pi a}\left(\sigma_s^{\max} - \sigma_s^{\min}\right) \tag{17}$$

Where, $\sigma_n^{\max}$ is the maximum value of normal stress, $\sigma_n^{\min}$ is the minimum value of normal stress, $\sigma_s^{\max}$ is the maximum value of shear stress, $\sigma_s^{\min}$ is the minimum value of shear stress.

When studying the single cracking problem of rectangular plates with contact shapes similar to those in DEM, Tada et al.[36] derived the formula for calculating the shape coefficients of type I cracking and type II cracking of rectangular plates, as shown in Eq. (18).

$$Y_I = Y_{II} = Y = \frac{1 - 0.025\left(\frac{a}{d}\right)^2 + 0.06\left(\frac{a}{d}\right)^4}{\sqrt{\cos\left(\frac{\pi a}{2d}\right)}} \tag{18}$$

By substituting Eq. (11) into Eq. (16-18), the following result is obtained:

$$\Delta K_I = Y\sqrt{\pi d\xi}\left(\sigma_n^{\max} - \sigma_n^{\min}\right) \tag{19}$$

$$\Delta K_{II} = Y\sqrt{\pi d\xi}\left(\sigma_s^{\max} - \sigma_s^{\min}\right) \tag{20}$$

$$Y = \frac{1 - 0.025\left(\xi\right)^2 + 0.06\left(\xi\right)^4}{\sqrt{\cos\left(\frac{\pi\xi}{2}\right)}} \tag{21}$$

Accordingly, the damage increment can be calculated using the damage rate and the contact diameter update time, as illustrated in Eq. (22). The real-time contact stress can be derived from Eq. (23), and the contact area can be determined from Eq. (24).

$$\Delta\xi = \frac{A\left(\Delta J\right)^n}{d}\Delta t \tag{22}$$

$$\sigma = \frac{F}{A} \tag{23}$$

$$A = d_0 \eta \tag{24}$$

Where, $\Delta\xi$ is damage increment, Δt is contact diameter update time, F is contact force between ball-ball, A is contact area between ball-ball, d_0 is initial value of contact diameter, η is contact thickness. In the PFC 2D, $\eta = 1$.

Furthermore, a damage criterion can be formulated based on the contact diameter and damage increment, thereby enabling the derivation of the improved Burgers model contact diameter expression, as illustrated in Eq. (25).

$$d = \begin{cases} d_0 & \sigma < \sigma_a \\ d_0 - \dfrac{A(\Delta J)^n}{d}\Delta t & \sigma_a < \sigma < \sigma_c \\ 0 & \sigma_c < \sigma \end{cases} \tag{25}$$

Where, σ is real-time contact stress, σ_a is damage initial stress, σ_c is contact break stress.

2.4 Implementation of fatigue damage models in DEM

First, a discrete element model of asphalt mortar was developed and brought to equilibrium. Upper and lower loading plates were then introduced to apply cyclic fatigue loads. The model was analyzed to compute the contact stress, which was determined by the relationship between contact force and contact diameter. The relationships among contact stress, damage initiation stress, and contact break stress were subsequently evaluated. Contacts that met the reduction criteria underwent contact diameter reduction. The procedure for damage reduction is outlined as follows:

(1) When $\sigma < \sigma_a$, the reduction condition is not satisfied and contact diameter not be changed.

(2) When $\sigma_a < \sigma < \sigma_c$, the reduction condition is satisfied. Firstly, the initial damage is defined as a small value 0.01%. thus ΔJ can be calculated according to Eq. (13). And reduction rate can be calculated according to Eq. (12). Then damage increment can be calculated by Eq. (22), and the updated contact diameter can be calculated by Eq. (25). At this time, the new contact stress can be calculated according to Eq. (23) and the judgment step of the next cycle can be entered. In the cycle process, if the reduction conditions are satisfied, the damage value of the last step is taken as the initial damage value of the current step, and the actual damage value of the current step is the sum of the initial damage value of the current step and the damage increment of the last step, as shown in Eq. (26).

$$\xi_i = \xi_{i-1} + \Delta\xi_{i-1} \tag{26}$$

Where, ξ_i is the damage value of current step, ξ_{i-1} is the damage value of last step, $\Delta\xi_{i-1}$ is the damage increment of last step. Particularly, for the first cycle, the initial damage ξ_0 is defined as 0.01%, the initial damage increment $\Delta\xi_0$ is 0.

(3) When $\sigma_c < \sigma$, the reduction condition is not satisfied. The contact breaks and no longer participates in the reduction cycle calculation.

The flow chart of damage program is shown in Fig. 6.

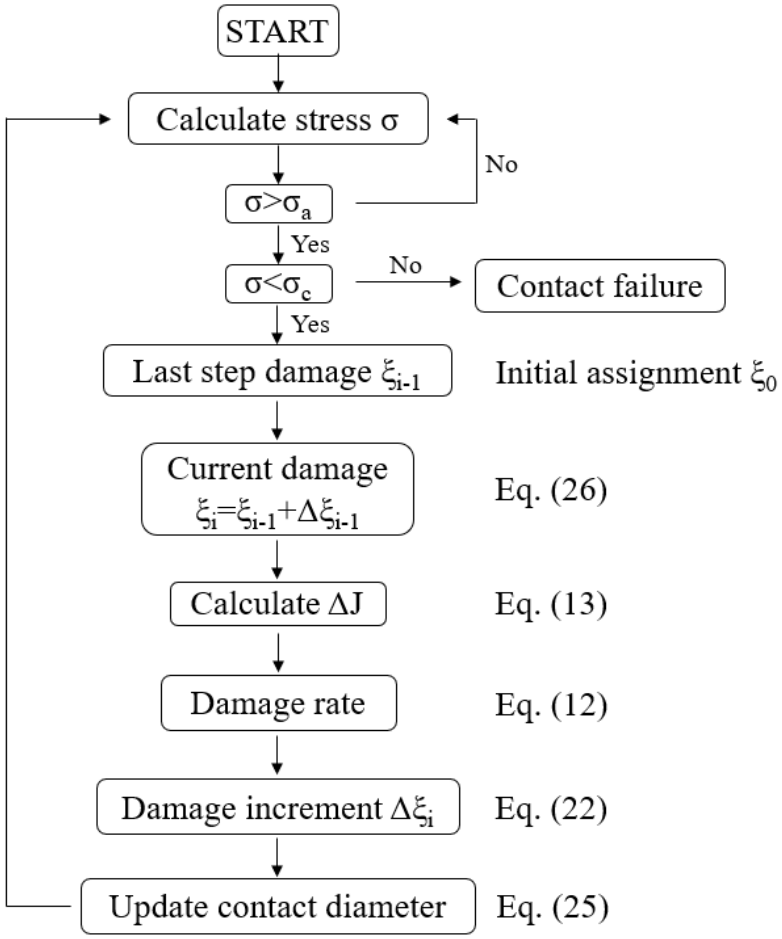

Fig. 6. Flow chart of fatigue damage evolution at particle interfaces in discrete element modeling

3 Materials and Methods

3.1 Materials and experiment

Asphalt mortar specimens were prepared using #70 virgin asphalt binder and SBS-modified asphalt binder, with their material properties listed in Table 1. The fine aggregates and fillers were made of limestone, with a maximum particle size of 4.75 mm. Table 2 presents the grading curve of the asphalt mortar. In this study, asphalt mortar, rather than asphalt mixture, was used to validate the discrete element viscoelastic fatigue damage model, as it provides more stable and consistent results along with enhanced computational efficiency.

Table 1. Parameters of #70 virgin and SBS modified asphalt binders

Test Item	Type of asphalt	
	#70 virgin asphalt binder	SBS modified asphalt binder
Penetration (25℃, 100g, 5s, 0.1mm)	70	57
Softening Point (℃)	47	66.8
Ductility (cm)	50.5 (10℃)	39.5 (5℃)

Table 2. Gradation of asphalt mortar

Sieving size/mm	**4.75**	**2.36**	**1.18**	**0.6**	**0.3**	**0.15**	**0.075**

Passing ratio/%	100	72	42	32	24	14	8

In this study, the uniaxial compressive dynamic modulus test was employed to determine the parameters of the Burgers model for asphalt mortar. Asphalt mortars were prepared using two different types of asphalt binders, and then cored and cut into specimens with a diameter of 100 mm and a height of 150 mm. The tests were conducted following the Dynamic Modulus Finger Print Test procedure in AASHTO TP 107[37]. The testing temperatures were set at 0°C, 10°C, 20°C, and 30°C, with testing frequencies of 0.1 Hz, 0.5 Hz, 1 Hz, 5 Hz, 10 Hz, and 25 Hz.

3.2 Viscoelastic properties of asphalt mortar

The Williams-Landel-ferry(WLF) equation is used to determine the time-temperature conversion coefficient[38], as shown in Eq. (27-28). The Sigmoidal model was selected to fit the master curve of the dynamic modulus[39], [40], as shown in Eq. (29).

$$\lg \alpha_T = \frac{-C_1 (T - T_0)}{C_2 + T - T_0} \tag{27}$$

$$f_r = f \cdot \alpha_T \tag{28}$$

$$\log\left(\left|E^*\right|\right) = \delta + \frac{\alpha}{1 + e^{\eta - \gamma \log(f_r)}} \tag{29}$$

Where, α_T is the time-temperature shift factor, C_1 and C_2 are fitting parameters, T is test temperature, T_0 is reference temperature, f_r is reduced frequency, δ is the minimum logarithm of the dynamic modulus, α is the span of the logarithm of the dynamic modulus, η and γ are shape parameters.

The reference temperature set in this study is 10℃, and the dynamic modulus of asphalt mortars prepared by two kinds of asphalt binders are shown in Fig. 7.

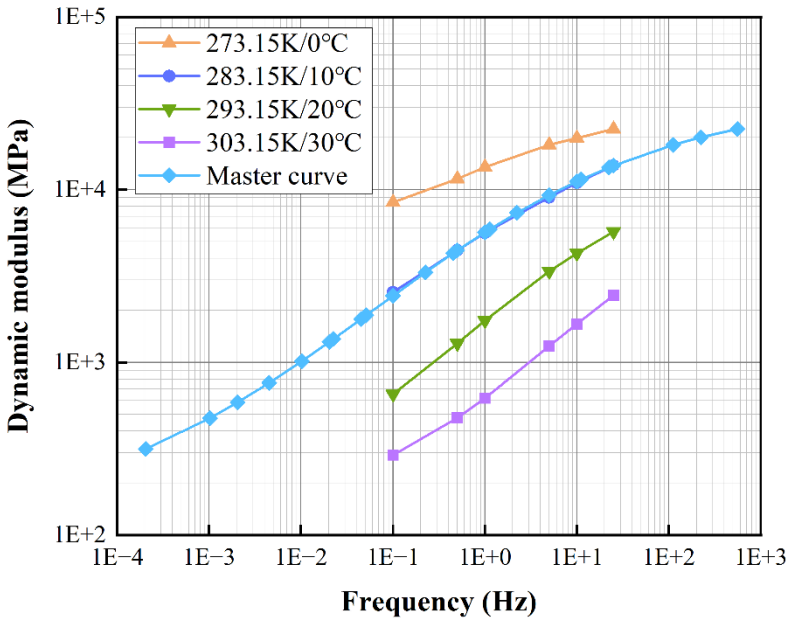

(a) #70 virgin asphalt mortar

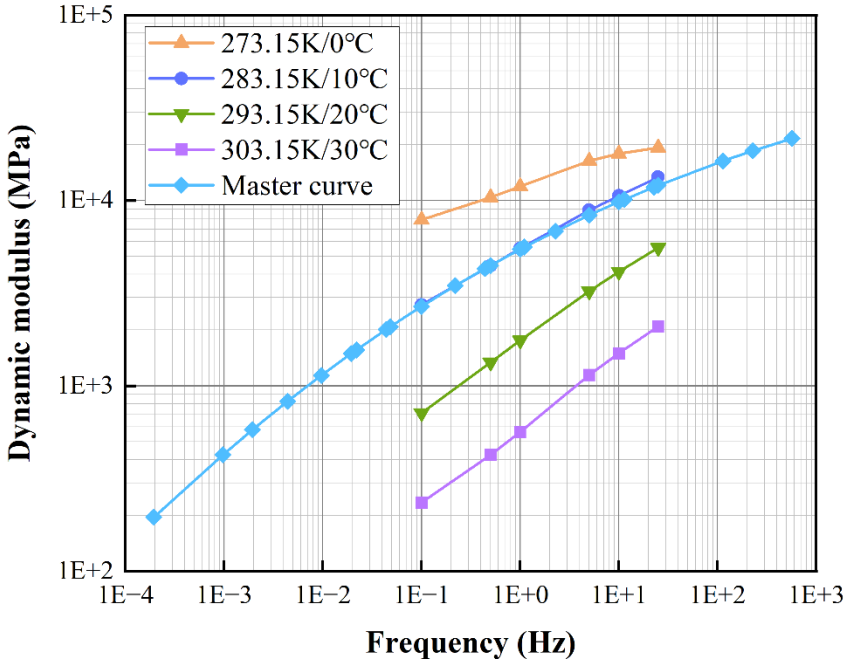

(b) SBS modified asphalt mortar

Fig. 7. Dynamic modulus master curve of asphalt mortar at 278.15K (10℃)

Generalized Maxwell model was used to characterize the viscoelastic properties of macroscopic asphalt mortar, and Prony series model was used to describe the relaxation modulus, as shown in Eq. (30).

$$E(t) = E_{\infty} + \sum_{i-1}^{M} E_m \exp\left(-\frac{t}{\tau_m}\right) \tag{30}$$

Where, E_{∞} is long-term equilibrium modulus, E_m is the components of the relaxation modulus, τ_m is the components of relaxation time, M is the total number of the Maxwell elements.

According to Zhang et al.[41], the relaxation modulus components can be determined by Eq. (31-32). The dynamic modulus can be determined according to Eq. (33).

$$E'(\omega) = E_{\infty} + \sum_{i=1}^{M} \frac{\omega^2 \tau_m^2 E_m}{1+\omega^2 \tau_m^2} \tag{31}$$

$$E''(\omega) = \sum_{i=1}^{M} \frac{\omega \tau_m E_m}{1+\omega^2 \tau_m^2} \tag{32}$$

$$\left|E^*(\omega)\right| = \sqrt{\left[E'(\omega)\right]^2 + \left[E''(\omega)\right]^2} \tag{33}$$

Where, $E'(\omega)$ is the storage modulus, $E''(\omega)$ is the loss modulus, ω is the angular frequency.

After constructing the master curve at the reference temperature, initial values for the long-term equilibrium modulus and relaxation modulus components were assigned. The storage modulus and loss modulus at different frequencies under the reference temperature were calculated, along with the dynamic modulus results derived from the generalized Maxwell model. The dynamic modulus results from the master curve were then compared with those from the generalized Maxwell model to establish an error metric. By minimizing this error through optimization, the

values of the long-term equilibrium modulus and relaxation modulus components were determined. This process yielded the mathematical expression of the relaxation modulus for the generalized Maxwell model at the reference temperature. Table 3 shows the relaxation modulus parameters of #70 virgin asphalt mortar and SBS modified asphalt mortar.

Table 3. Relaxation modulus parameters of Prony series model for asphalt mortar

Long-term modulus E_m (MPa)			Components of relaxation time τ_m (s)	
Type of asphalt	#70	SBS		
E_∞	52.0	48.2		
E_1	501.2	501.0	τ_1	0.00001
E_2	852.5	835.4	τ_2	0.0001
E_3	8021.9	5041.5	τ_3	0.001
E_4	6681.1	6347.0	τ_4	0.01
E_5	4463.4	4545.6	τ_5	0.1
E_6	2127.3	1845.2	τ_6	1
E_7	895.5	1085.8	τ_7	10
E_8	296.1	314.9	τ_8	100
E_9	263.1	199.1	τ_9	1000
E_{10}	4.73	4.69	τ_{10}	10000
E_{11}	2.95	2.94	τ_{11}	100000

3.3 Determining Burgers model parameters from dynamic modulus tests

However, the generalized Maxwell viscoelastic model is not integrated into the PFC software. Therefore, in this study, the macroscopic parameters of the Burgers model were obtained by fitting its relaxation modulus to that of the generalized Maxwell model. The expression for the relaxation modulus of the Burgers model is provided in Eq. (34). Upon obtaining the mathematical expressions for the relaxation modulus of the generalized Maxwell model for different types of asphalt mortar at the reference temperature, the fundamental parameters in the Burgers model's relaxation modulus expression were assumed. An R-squared error fitting analysis was performed between the relaxation moduli of the two models, as shown in Eq. (35). By optimizing the parameters to achieve R-squared values approaching 1, the essential parameters of the Burgers model's relaxation modulus expression were determined, and the macroscopic parameters of the Burgers model were subsequently calculated.

$$E(t)=\frac{1}{\sqrt{p_1^2-4p_2}}\times\left[\left(-q_1+\alpha q_2\right)e^{-\alpha t}+\left(q_1-\beta q_2\right)e^{-\beta t}\right]$$

$$p_1=\frac{\eta_1}{E_1}+\frac{\eta_1+\eta_2}{E_2}$$

$$p_2=\frac{\eta_1\eta_2}{E_1E_2}$$

$$q_1=\eta_1 \tag{34}$$

$$q_2=\frac{\eta_1\eta_2}{E_2}$$

$$\alpha=\frac{1}{2p_2}\left(p_1+\sqrt{p_1^2-4p_2}\right)$$

$$\beta=\frac{1}{2p_2}\left(p_1-\sqrt{p_1^2-4p_2}\right)$$

$$R^2=1-\frac{\sum_{i=1}^{n}\left(\hat{y}_i-y_i\right)^2}{\sum_{i=1}^{n}\left(\overline{y_i}-y_i\right)^2} \tag{35}$$

Where, η_1 is the viscosity of Maxwell model, η_2 is the viscosity of Kelvin model, E_1 is the elastic modulus of Maxwell model, E_2 is the elastic modulus of Kelvin model, $\hat{y}_i$ is the predicted value, y_i is the true value, $\overline{y_i}$ is the mean value.

By fitting the generalized Maxwell relaxation modulus and the Burgers relaxation modulus with R^2 error, the macroscopic Burgers model parameters of the two asphalt mortars can be obtained, as shown in Table 4. Assuming a Poisson's ratio of 0.4 for the asphalt mortar, the microscopic Burgers model parameters can be derived by substituting the macroscopic parameters into Eq. (3-10), as shown in Table 5.

Table 4. Burgers model parameters of asphalt mortar at the macroscale

Type of asphalt mortar	E_1/Pa	$\eta_1/Pa\cdot s$	E_2/Pa	$\eta_2/Pa\cdot s$
#70 virgin asphalt mortar	5.66e9	5.94e10	1.80e9	4.34e9
SBS modified asphalt mortar	4.60e9	5.99e10	1.97e9	5.02e9

Table 5. Burgers model parameters of asphalt mortar at the microscale interfaces

Type of asphalt	k_{mn} $Pa\cdot m$	c_{mn} $Pa\cdot m\cdot s$	k_{kn} $Pa\cdot m$	c_{kn} $Pa\cdot m\cdot s$	k_{ms} $Pa\cdot m$	c_{ms} $Pa\cdot m\cdot s$	k_{ks} $Pa\cdot m$	c_{ks} $Pa\cdot m\cdot s$
#70	1.13e10	1.19e11	3.60e9	8.68e9	4.04e9	4.24e10	1.29e9	3.10e9
SBS	9.20e9	1.20e11	3.94e9	1e10	3.29e9	4.28e10	1.41e9	3.59e9

3.4 Determining fatigue model parameters using indirect tensile fatigue tests

In the laboratory, indirect tensile fatigue tests were conducted on #70 asphalt mortar and SBS asphalt mortar at three stress levels (550kPa, 650kPa, and 750kPa) with a loading frequency of 10 Hz. Simultaneously, a virtual indirect tensile fatigue test model for asphalt mortar was developed in PFC. The loading head was set to stress-control mode to maintain consistent loading and stress levels,

replicating the parameters of the laboratory tests. The fatigue life of the asphalt mortar in the indirect tensile test was defined as the number of loading cycles required to achieve a 50% reduction in modulus. In the virtual test, the stress level was initially set to 650kPa for the #70 asphalt mortar, enabling the calibration of parameters A, n, and initial cracking stress σ_a based on the fatigue life observed at the 650kPa stress level in the experimental test. The calibration method for SBS asphalt mortar followed the same procedure as for #70 asphalt mortar. Table 6 presents the calibration results for both asphalt mortars, where the contact break stress σ_c is defined as the splitting strength from the indirect tensile strength test.

Table 6. Calibrated damage parameters of different asphalt mortar types

Type of asphalt mortar	A	n	σ_a /Pa	σ_c /Pa
#70 virgin asphalt mortar	3.51e-7	0.51	4e4	1.933e6
SBS modified asphalt mortar	5.96e-7	0.69	4e4	1.857e6

4 Results and discussion

4.1 Validating improved Burgers model predictions using indirect tensile dynamic modulus tests

To validate the accuracy of the microscopic parameters of the improved Burgers model, an indirect tensile dynamic modulus test was conducted. Two types of asphalt mortar specimens were prepared in the laboratory and cut into samples with a diameter of 100 mm and a thickness of 40 mm. The IDT dynamic modulus test was carried out using a DTS machine under controlled conditions: a temperature of 10°C and frequencies of 1 Hz, 3 Hz, 5 Hz, and 10 Hz. This produced the actual IDT dynamic modulus values. In parallel, a virtual IDT dynamic modulus test was simulated in PFC, using the microscopic parameters from Table 5 and applying the same loading frequencies of 1 Hz, 3 Hz, 5 Hz, and 10 Hz. As shown in Eq. (36), the error between the experimented dynamic modulus and the simulated dynamic modulus is calculated. Table 7 presents the actual and simulated IDT dynamic modulus values for both types of asphalt mortars, as well as the associated errors. The findings confirm that the microscopic parameters of the improved Burgers model are accurate and reliable, making them suitable for use in studying IDT fatigue damage via discrete element methods.

$$Error = \left| \frac{E_{Experiment} - E_{Simulation}}{E_{Experiment}} \right| \tag{36}$$

Where, $E_{Experiment}$ is experimented dynamic modulus, $E_{Simulation}$ is simulated dynamic modulus.

Table 7. Validation of IDT dynamic modulus between experiment and simulation

Type of asphalt	Frequency (Hz)	Experiment (MPa)	Simulation (MPa)	Error (%)
#70	1	6439	5691	11.62
	3	10161	9227	9.19
	5	12982	11759	9.42
	10	15671	14553	7.13
SBS	1	5451	5782	6.07
	3	7703	8339	8.26
	5	8592	9065	5.51
	10	11609	11845	2.03

4.2 Validating DEM fatigue evolution model predictions using indirect tensile fatigue tests

In the virtual indirect tensile fatigue test, stress levels were set at 550kPa and 750kPa. The calibrated model parameters from the 650kPa stress level were applied to predict the virtual fatigue life results at the 550kPa and 750kPa stress levels. Fig. 8 compares the experimental and simulated fatigue life of the two asphalt mortars under different stress levels. As shown in Fig. 8, the simulated fatigue life of the #70 asphalt mortar and the SBS asphalt mortar closely matches the laboratory results, indicating that the fatigue damage parameters A, n, and the initial cracking stress σ_a are accurately estimated.

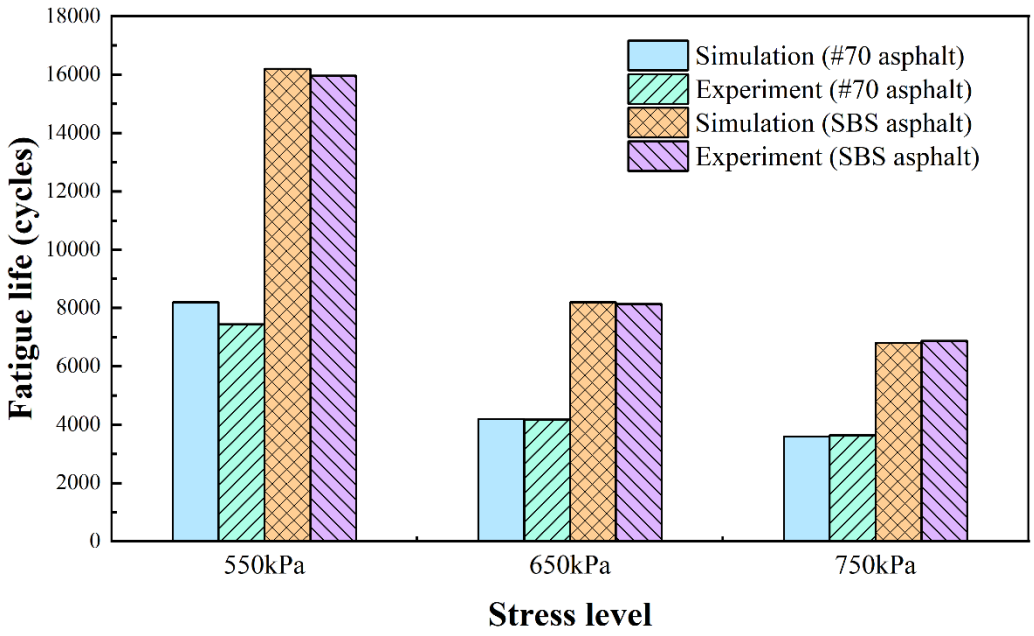

Fig. 8. The fatigue lives of experiment and simulation at different asphalt types and stress levels

Fig. 9 illustrates the simulated and experimental crack growth in #70 asphalt mortar and SBS asphalt mortar subjected to varying fatigue cycles at a stress level of 650kPa. In the simulation, red lines represent instances where contact was broken due to fatigue damage under cyclic loading. A cluster of adjacent red lines indicates the cracking area in the asphalt mortar under simulated indirect tensile fatigue loading. To observe crack formation and propagation more clearly, a layer of gypsum was applied to the surface of the asphalt mortar in the laboratory tests. After 3800 cycles for the #70 asphalt mortar and 7800 cycles for the SBS asphalt mortar, minor cracks appeared in both the upper and lower sections. As the number of load cycles increased, the number, length, and width of cracks in both mortars also increased. Additionally, a comparison of the two mortars shows that SBS asphalt mortar withstood a greater number of cycles before reaching the same level of cracking as the #70 asphalt mortar. This is due to the strong adsorption effect of the SBS polymer on the oil content in the asphalt, combined with its swelling, expansion, and molecular chain extension. Ultimately, the SBS polymer forms a continuous network structure, with asphalt particles distributed within it[42], [43]. As cracks form and propagate, the polymer network inhibits their spread to some extent, significantly enhancing the fatigue resistance of SBS asphalt mortar compared to #70 asphalt

mortar.

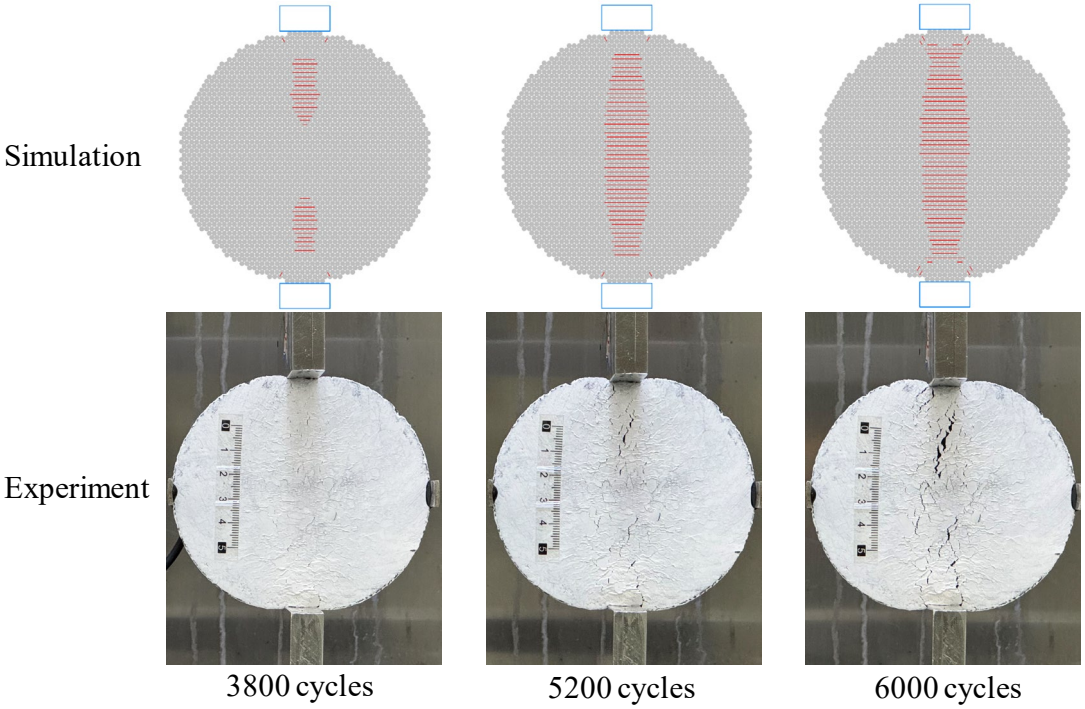

(a) #70 asphalt mortar

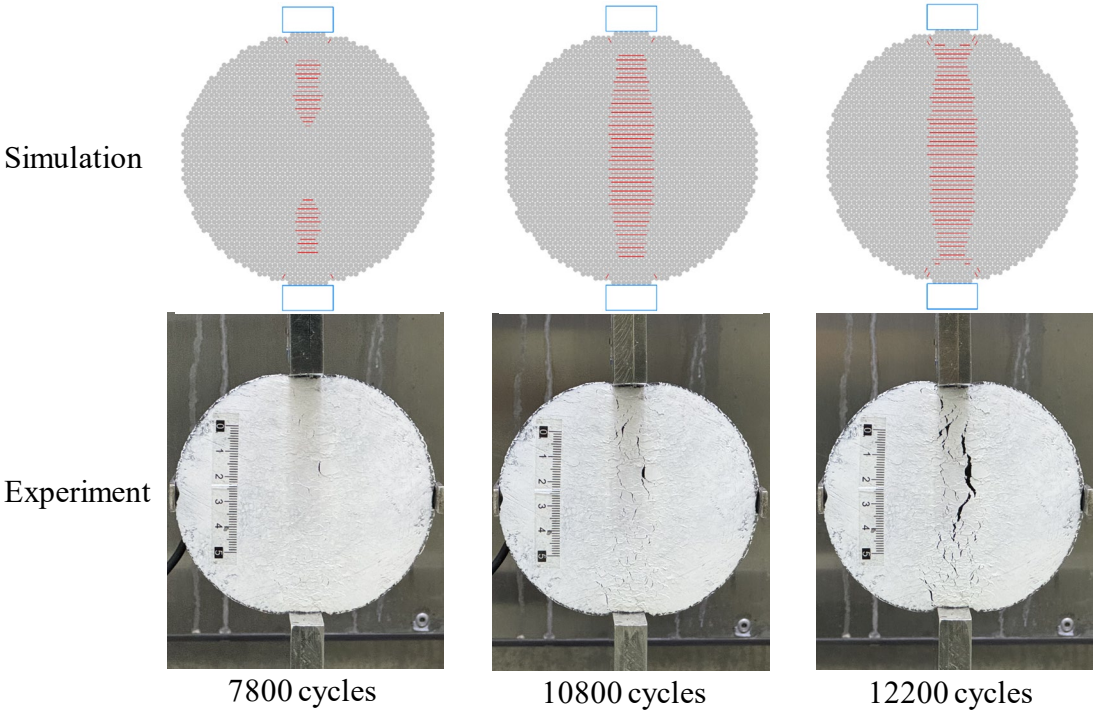

(b) SBS asphalt mortar

Fig. 9. Crack growth of simulation and experiment at different asphalt types: (a) #70 asphalt mortar; (b) SBS asphalt mortar.

Fig. 10 illustrates the definition and methodology for quantifying the surface crack area of asphalt mortar. During fatigue loading, numerous minor cracks form on the asphalt mortar surface.

This study introduces a definition for the surface crack area: if the distance between two adjacent cracks is less than 5 mm, the region between them is considered part of the crack area. If there are no nearby cracks, the crack area is defined as the region of the crack itself. In Fig. 10, the crack area is highlighted in red according to this definition. The methodology involves identifying each crack in the image, defining the crack area through image processing techniques, and calculating the equivalent surface crack area based on a ratio measurement. The definition and methodology for quantifying the surface crack area was applied to processing the images from experiments and simulations to generate the crack areas.

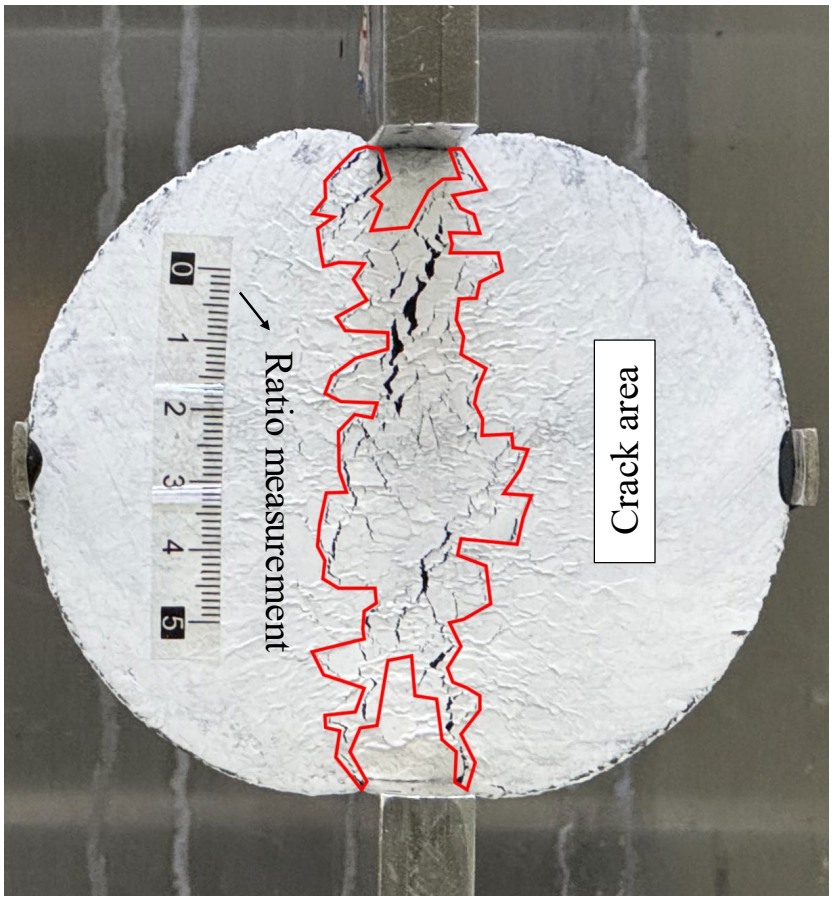

Fig. 10. Surface crack area definition and measurement of asphalt mortar

The length of each red line in the simulation section of Fig. 9 can be derived from the DEM as a ratio measurement. The simulated crack area is then calculated using image processing techniques. The methodology shown in Fig. 10 is applied to compute the equivalent surface crack area of two distinct asphalt mortars subjected to varying indirect tensile fatigue load cycles. The crack area obtained from DEM simulation under the same conditions is compared with the experimental data. The resulting calculation error is illustrated in Fig. 11. It can be observed that the discrepancy between the simulated and experimental crack areas, across different asphalt types and loading cycles, is less than 15%. This demonstrates that discrete element indirect tensile fatigue test simulation can effectively reflect the actual crack growth.

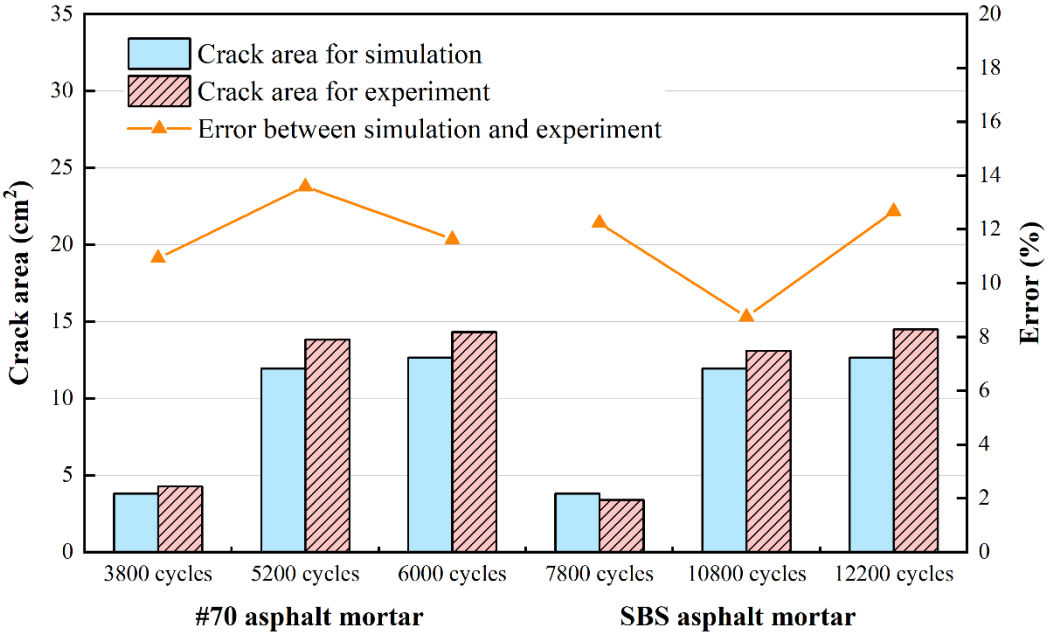

Fig. 11. Crack area and error of simulation and experiment at different asphalt types and indirect tensile fatigue load cycles

4.3 Crack growth in indirect tensile fatigue tests at the microscale

Fig. 12 demonstrates the crack growth in various asphalt types under different stress levels and loading cycles. For this analysis, #70 asphalt mortar under a stress level of 650kPa was selected as a case study. After 3400 cycles, the contact between the upper and lower parts of the asphalt mortar was severed. Near the loading head, lateral contact failure occurred due to localized stress concentrations during force transmission. By 3800 cycles, cracks in the upper and lower regions began to gradually extend toward both the loading head and intermediate areas. Crack propagation toward the sides of the loading head was relatively slow, while it occurred more rapidly toward the middle region. At 4200 cycles, the upper and lower cracks converged in the middle region, and the original crack area began expanding laterally. By 5200 cycles, the lateral crack expansion continued. By 6000 cycles, the cracks had propagated toward the loading head area on both sides, forming a full-depth crack from top to bottom. The middle portion of this penetrating crack appeared wider, tapering gradually toward both ends. Additionally, localized widening of the crack was observed due to changes in stress distribution near the loading head. Importantly, no fatigue cracks were detected in the triangular region near the loading head, which aligns with the findings from experimental tests.

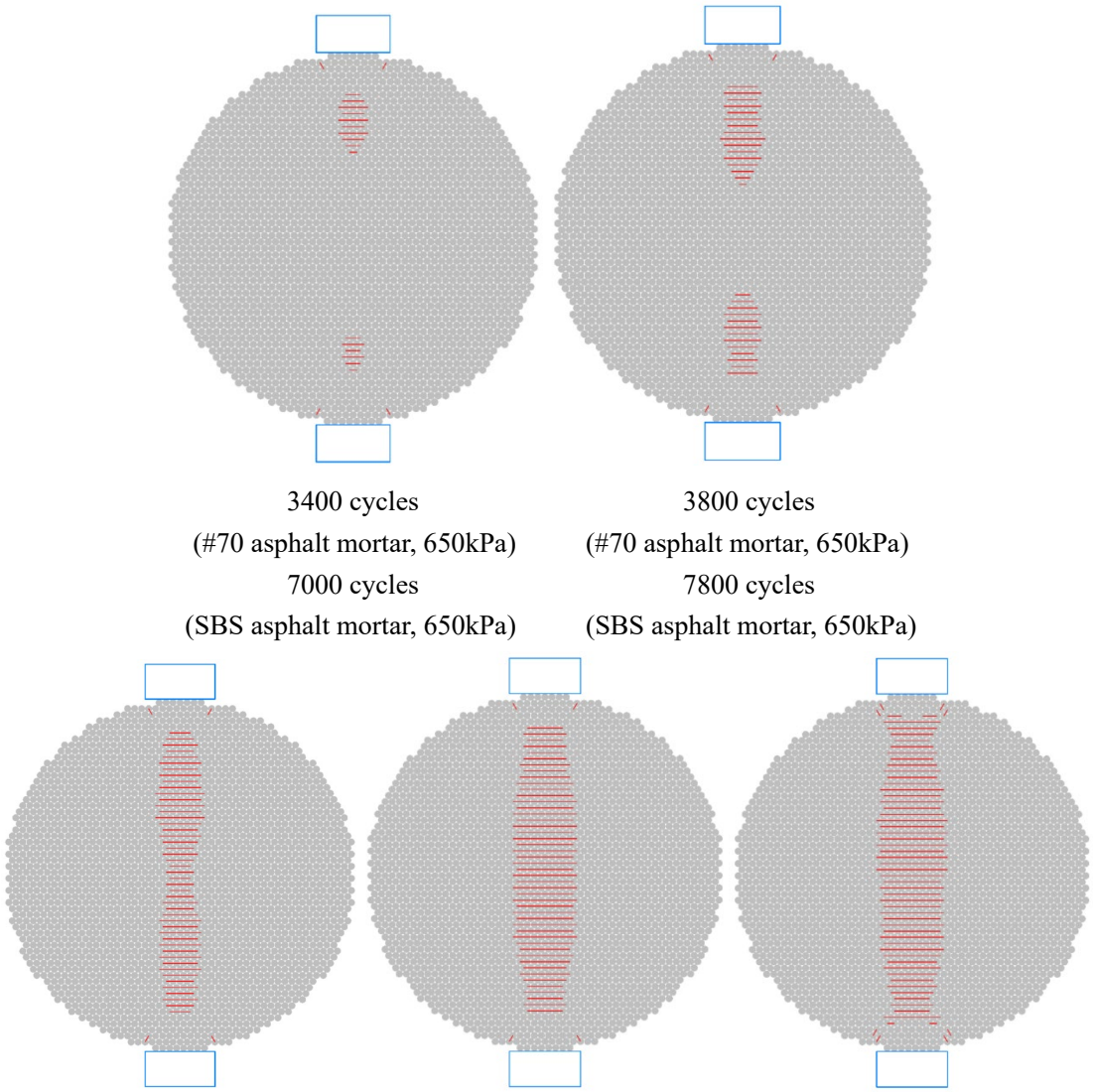

Fig. 12. The microscopic crack growth of different asphalt types and indirect tensile fatigue load cycles.

Moreover, an increase in stress level correlates with an accelerated rate of crack growth in the same asphalt mortar. This occurs because higher stress levels intensify the internal contact forces within the asphalt mortar, thereby expediting damage accumulation. This accelerated accumulation of damage ultimately results in a faster contact failure, as evidenced by the increased crack growth rate. Furthermore, when the stress level remains constant, the crack growth rate in SBS asphalt mortar is slower compared to that in #70 asphalt mortar. This disparity is attributed to differences in parameters A, n, and the representative modulus between the two asphalt materials. These variations lead to different rates of damage progression, causing the observed differences in crack growth rates. As a result, SBS asphalt mortar exhibits superior fatigue resistance.

4.4 Microstructural behavior analysis of fatigue crack growth in viscoelastic asphalt materials

Fig. 13 illustrates the directional changes in particle displacement within #70 asphalt mortar under varying cycles at a stress level of 650kPa. The red line indicates the contacts between particles that have been severed, with the area enclosed by the red line representing the cracked region. After 1000 cycles, particles along the vertical midline of the asphalt mortar exhibited upward displacement, aligning with the direction of force transmission. On both sides of the vertical midline, the displacement direction of particles gradually deviated toward the horizontal as the distance increased. By 3400 and 3800 cycles, partial cracking occurred in the upper and lower regions of the asphalt mortar. At this stage, compared to the assessment at 1000 cycles, the particle displacement on both sides had become more horizontal. This observation suggests that as the fatigue cycle load increases, horizontal displacement becomes more pronounced than vertical displacement. Additionally, as the number of fatigue cycles increases, the displacement direction of particles on both sides of the upper and lower cracks becomes increasingly skewed. This phenomenon occurs because crack formation hinders the horizontal transfer of force in the original region, resulting in greater horizontal forces exerted on particles adjacent to the cracks, thereby altering their displacement direction. In contrast, the displacement direction of particles in the central region remains similar to that observed during the initial loading period, as no cracks have yet formed. By 4200, 5200, and 6000 cycles, the upper and lower cracks had connected, and the particle displacement direction significantly changed on both sides of the fracture region. Similarly, as the number of fatigue cycles and the crack area increased, particle displacement on both sides became increasingly horizontal.

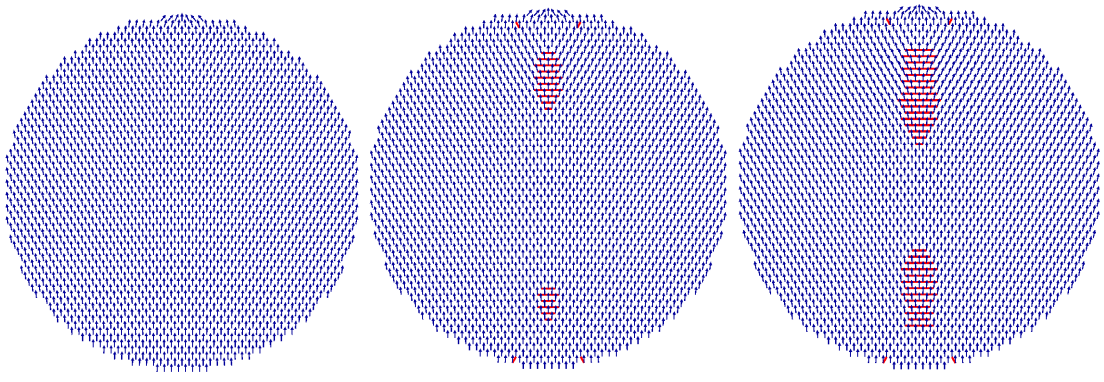

(a) 1000 cycles (b) 3400 cycles (c) 3800 cycles

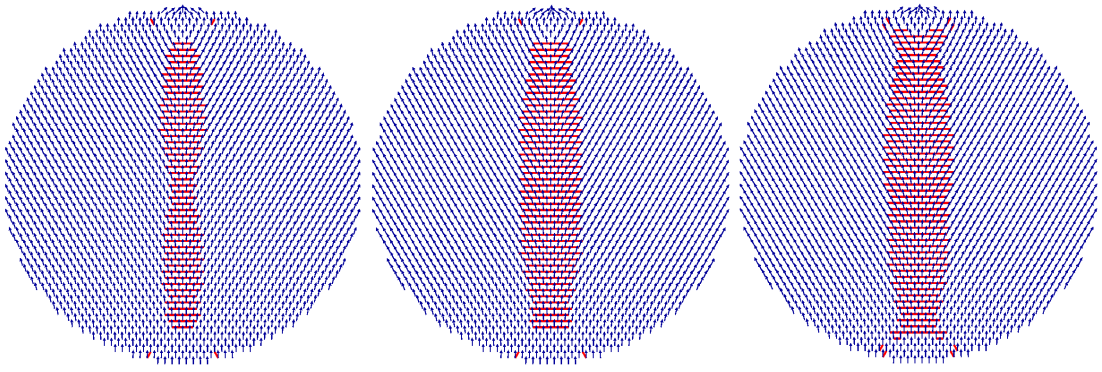

(d) 4200 cycles (e) 5200 cycles (f)6000 cycles

Fig. 13. Particle displacement direction of #70 asphalt mortar and 650kPa stress level at different indirect tensile fatigue load cycles

Fig. 14 illustrates the magnitude of horizontal particle displacement under varying fatigue cycle loads. Blue indicates leftward displacement, while red represents rightward displacement, with darker shades corresponding to greater magnitudes of displacement. After 1000 cycles, displacements are observed on both the left and right sides of the vertical midline, exhibiting leftward and rightward movements in their respective directions. As the distance from the vertical midline increases, the displacements become more pronounced. The green area in the center of the graph indicates relatively minor horizontal displacement, with its horizontal extent largely consistent with the contact range of the loading head, reflecting the force transmission process. By 3400 cycles, cracks have formed in the upper and lower portions of the asphalt mortar, resulting in more pronounced displacements on both sides of the cracks, while the central region exhibits relatively minor changes. This is due to localized stress concentrations induced by the cracks, which intensify the horizontal forces exerted on particles adjacent to the cracks. At 3800 cycles, the cracks in the upper and lower portions of the asphalt mortar expanded further, accompanied by more pronounced horizontal displacement on both sides. By 4200 cycles, the upper and lower cracks coalesced, forming a long, narrow zone of relatively minor displacement, with discernible changes in horizontal displacement on either side. At 5200 and 6000 cycles, the region of relatively minor intermediate displacement gradually expanded as the fracture width and length increased.

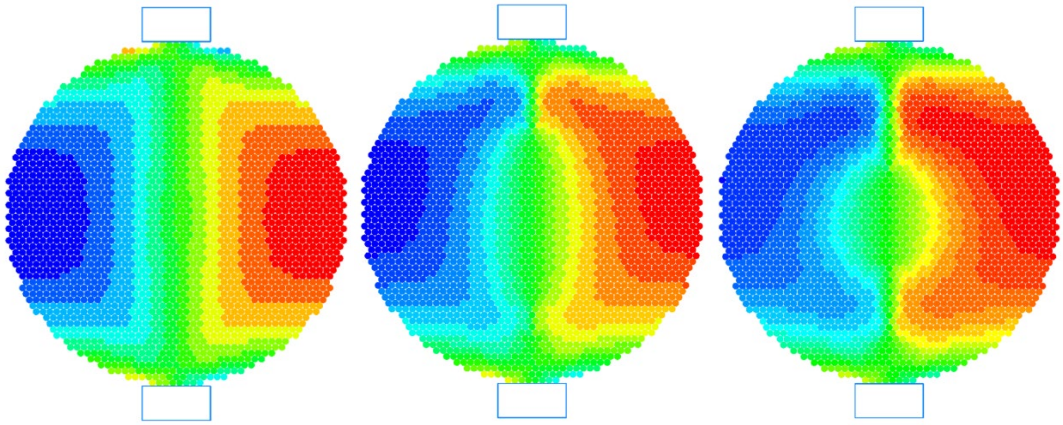

(a) 1000 cycles (b) 3400 cycles (c) 3800 cycles

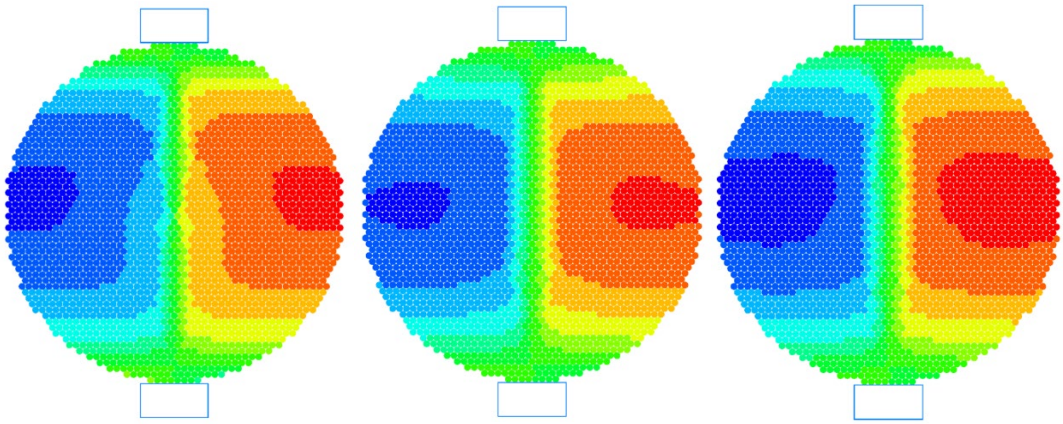

(d) 4200 cycles (e) 5200 cycles (f) 6000 cycles

Fig. 14. Particle horizontal displacement magnitude of #70 asphalt mortar and 650kPa stress level at different indirect tensile fatigue load cycles

Fig. 15 illustrates the force chain in #70 asphalt mortar under varying durations of cyclic loading at a stress level of 650kPa. Blue represents compressive forces, while green indicates tensile forces. After 1000 cycles, the asphalt mortar exhibits vertical compression and horizontal tension. However, in the upper left, lower left, upper right, and lower right quadrants, horizontal compression occurs due to force transfer. Compressive forces arise along the direction of force conduction, whereas tensile forces emerge when force conduction is perpendicular to this direction. A "meniscus" pattern also forms at the junctions between these quadrants and the central region, where horizontal tension occurs when force conduction aligns with the horizontal axis, and compression arises when it is perpendicular. This phenomenon is mainly attributed to the overall force conduction during cyclic fatigue loading, which primarily moves from the upper and lower sides toward the central region. In the four corner regions, however, the force conduction deviates, leading to distinct tensile and compressive behavior in different directions. At these junctions, the deviation also induces partial tension and compression. Additionally, a small localized area beneath the loading head experiences both horizontal and vertical compression due to localized stress concentrations. At 3400 and 3800 cycles, crack formation causes the horizontal force in the affected area to disappear, while vertical compression persists. The "meniscus" region shifts toward the center, and compression zones develop on either side of the crack. This shift results from alterations in the force conduction path caused by the crack, leading to localized stress concentrations. At 4200, 5200, and 6000 cycles, the upper and lower cracks merge, causing the central region of the crack to transition from vertical compression to tension. Simultaneously, horizontal and vertical compression develop on the left and right sides of the asphalt mortar. Vertical tension and horizontal compression also emerge along the mortar's edges due to the formation of a penetrating crack, which weakens the mortar's integrity, resulting in stress concentrations and altering the compression and tension at the contact points.

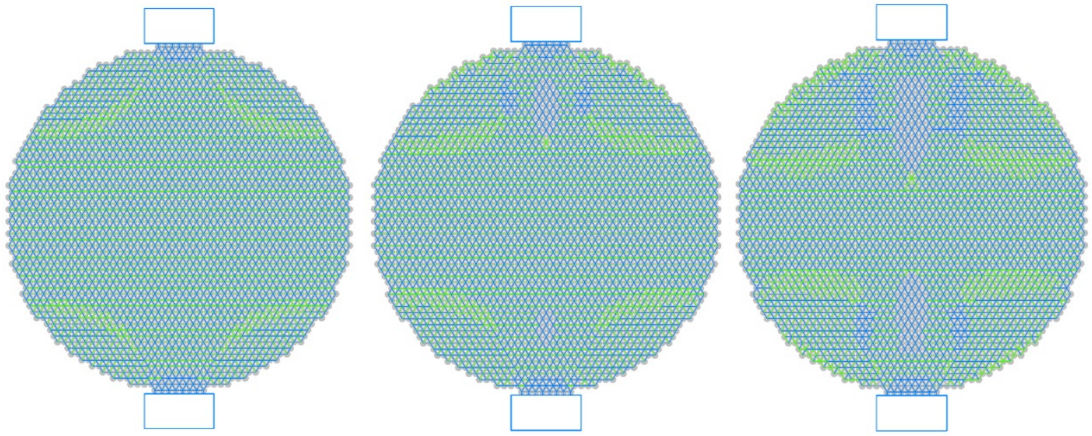

(a) 1000 cycles (b) 3400 cycles (c) 3800 cycles

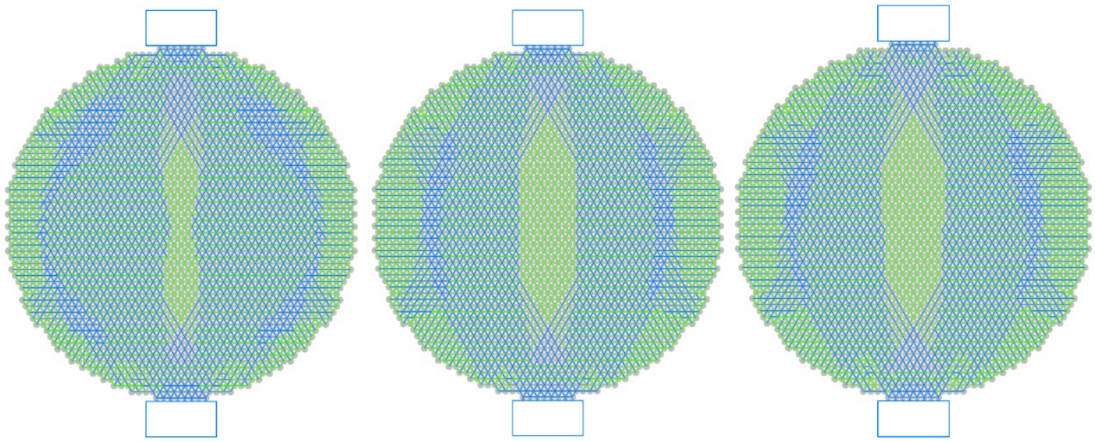

(d) 4200 cycles (e) 5200 cycles (f) 6000 cycles

Fig. 15. Force chain of #70 asphalt mortar and 650kPa stress level at different indirect tensile fatigue load cycles

Fig. 16 illustrates the contact break behavior of #70 asphalt mortar and SBS asphalt mortar under varying stress levels. For both asphalt materials, an increase in stress level reduces the number of fatigue load cycles before the onset of contact break. This is because the contact break stress is fixed for a given material. As stress levels rise, contact damage initiates earlier, leading to an earlier attainment of the contact break threshold, resulting in contact break. Additionally, higher stress levels significantly reduce the time between the onset of contact break and fatigue failure. At equivalent stress levels, the contact break patterns of #70 asphalt mortar and SBS asphalt mortar are generally similar. However, SBS asphalt mortar experiences more load cycles before the onset of contact break and exhibits a slower rate of break progression compared to #70 asphalt mortar. Specifically, at a stress level of 750kPa, the contact break rate remains relatively stable from the onset, with minimal fluctuations. At 650kPa, the contact break rate starts rapidly but stabilizes later. At 550kPa, the contact break rate is initially slow but accelerates in the later stages.

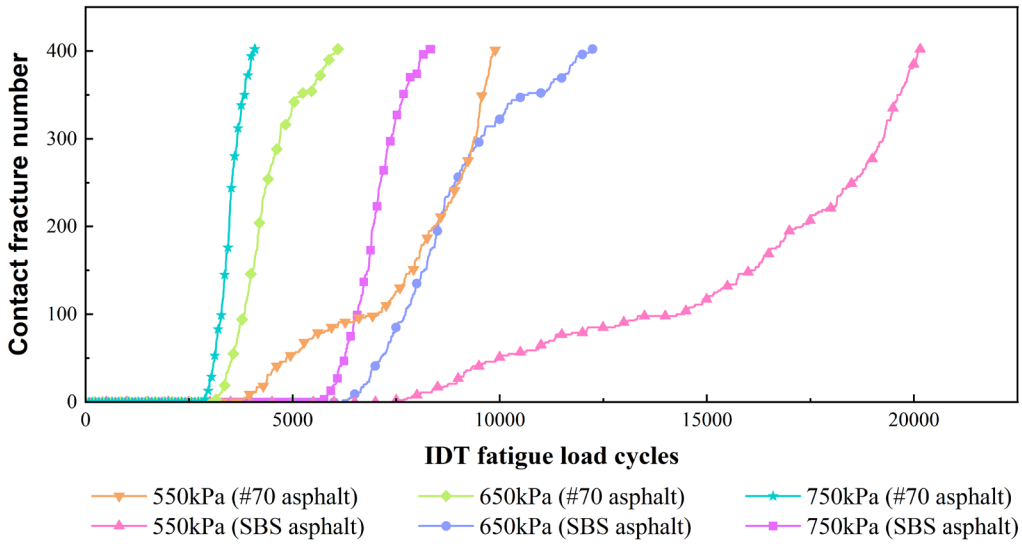

Fig. 16. The contact break condition of #70 asphalt mortar and SBS asphalt mortar under different stress levels.

5 Conclusions

In this study, the Burgers model within the PFC discrete element program was enhanced to incorporate bonding functionality by configuring the contact key and enabling contact deletion through the 'Fish' scripting language. Further improvements were made to the Burgers model to withstand tensile forces under repeated loading. The generalized Maxwell model was employed to characterize the viscoelastic relaxation modulus, with uniaxial compressive dynamic modulus tests conducted on asphalt mortar to determine the model parameters. The coefficients of the improved Burgers model were then calibrated using the relaxation modulus data. A microscale viscoelastic fatigue damage model was developed using the J-integral, based on Paris' law, to represent microscopic fatigue damage by reducing the particle contact diameter. This approach addresses limitations in existing fatigue damage models, where damage evolution is often empirically modeled through interparticle stresses or forces. Finally, an indirect tensile fatigue test of the asphalt mortar was conducted experimentally and simulated numerically using the proposed viscoelastic fatigue damage model. Main conclusions are as follows:

(1) The results of the indirect tensile dynamic modulus experiment and corresponding simulations at different frequencies were compared, with an average error of less than 10%. This validates the reliability of the microscopic parameters obtained using the proposed method.

(2) The fatigue life and crack area of #70 virgin asphalt and SBS-modified asphalt under varying stress levels were accurately evaluated through indirect tensile fatigue tests, along with the calibration of microscopic damage parameters. It was found that the damage parameters A and n for #70 virgin asphalt were lower than those for SBS-modified asphalt, with the crack area error within 15%.

(3) In the simulation of microscopic indirect tensile fatigue damage, crack formation impedes the horizontal transfer of force within the crack region, leading to stress concentration on particles adjacent to the crack and significantly increasing the relative displacement of these particles.

(4) During crack coalescence in the upper and lower regions, a pronounced tension-compression transformation occurs in the specimen’s edge regions. This phenomenon arises from transverse contact failure in the central part of the specimen after the cracks in the upper and lower regions interconnect. The contact failure disrupts the force transmission pathway, causing a notable reduction in the specimen's effective load-bearing area. Consequently, the interconnection of the upper and lower cracks signifies a substantial degradation in the specimen’s load-bearing capacity.

(5) The trend in the number of contact break with fatigue load cycles is independent of the asphalt type but is influenced by the stress level. This is primarily due to changes in stress level, which modify the number of contact break undergoing damage reduction at the same ratio (the number of fatigue load cycles as a proportion of total fatigue load cycles), thereby affecting the number of contact break. In contrast, variations in asphalt type only alter the damage parameters A and n, impacting the rate of contact break without affecting the overall trend.

The current study exhibits certain limitations, including the absence of validation for the fatigue damage model's accuracy under high-frequency and low-frequency loading regimes. Furthermore, given the pronounced temperature-dependent behavior of asphalt materials,

subsequent investigations could explore the model's adaptability to varying thermal conditions and even extend to environmental factors such as humidity and freeze-thaw cycles. Additionally, the effects of oxidative aging, UV aging and chemical aging of asphalt materials on the accuracy of the model can be further explored. In subsequent phases, this framework can be extended to fatigue damage simulations of asphalt mixtures incorporating diverse aggregate types, binder contents, and modification levels, thereby enhancing the generalizability of the viscoelastic fatigue damage model. In the future, this model can be applied to predict the fatigue life of asphalt pavements under varying loading magnitudes and environmental conditions, providing critical references for early detection of pavement distresses and implementation of preventive maintenance strategies. Additionally, during the pavement design phase, the model enables comparative evaluation of fatigue resistance across different material compositions and structural configurations. By simulating stress distributions at particle interfaces and crack propagation trajectories, it facilitates optimization of material formulations and structural designs to enhance the overall performance of pavement systems.

6 Acknowledgments

This paper is supported by the Engineering and Physical Sciences Research Council (EPSRC) under Grant number: EP/W000334/1 & EP/W000369/1, the National Natural Science Foundation of China under Grant No. 52478450, and the Start-up Research Fund of Southeast University (RF1028623231).

Reference

[1] P. A. Cundall, “A Computer Model for Simulating Progressive, Large-Scale Movement in Blocky Rock System,” in Symposium of the International Society for Rock Mechanics, 1971.

[2] K.-N. G. Chang and J. N. Meegoda, “Micromechanical Simulation of Hot Mix Asphalt,” *J. Eng. Mech.*, vol. 123, no. 5, pp. 495–503, May 1997, doi: 10.1061/(ASCE)0733-9399(1997)123:5(495).

[3] A. C. Collop, G. R. McDowell, and Y. W. Lee, “Modelling dilation in an idealised asphalt mixture using discrete element modelling,” *Granular Matter*, vol. 8, no. 3–4, pp. 175–184, Aug. 2006, doi: 10.1007/s10035-006-0013-3.

[4] H. Kim, M. P. Wagoner, and W. G. Buttlar, “Simulation of Fracture Behavior in Asphalt Concrete Using a Heterogeneous Cohesive Zone Discrete Element Model,” *J. Mater. Civ. Eng.*, vol. 20, no. 8, pp. 552–563, Aug. 2008, doi: 10.1061/(ASCE)0899-1561(2008)20:8(552).

[5] Y. Liu, Q. Dai, and Z. You, “Viscoelastic Model for Discrete Element Simulation of Asphalt Mixtures,” *J. Eng. Mech.*, vol. 135, no. 4, pp. 324–333, Apr. 2009, doi: 10.1061/(ASCE)0733-9399(2009)135:4(324).

[6] E. Mahmoud, E. Masad, and S. Nazarian, “Discrete Element Analysis of the Influences of Aggregate Properties and Internal Structure on Fracture in Asphalt Mixtures,” *J. Mater. Civ. Eng.*, vol. 22, no. 1, pp. 10–20, Jan. 2010, doi: 10.1061/(ASCE)MT.1943-5533.0000005.

[7] Y. Liu, Z. You, and Y. Zhao, “Three-dimensional discrete element modeling of asphalt concrete: Size effects of elements,” *Construction and Building Materials*, vol. 37, pp. 775–782, Dec. 2012, doi: 10.1016/j.conbuildmat.2012.08.007.

[8] T. Ma, D. Zhang, Y. Zhang, and J. Hong, "Micromechanical response of aggregate skeleton within asphalt mixture based on virtual simulation of wheel tracking test," *Construction and Building Materials*, vol. 111, pp. 153–163, May 2016, doi: 10.1016/j.conbuildmat.2016.02.104.

[9] J. Chen, B. Huang, and X. Shu, "Air-Void Distribution Analysis of Asphalt Mixture Using Discrete Element Method," *J. Mater. Civ. Eng.*, vol. 25, no. 10, pp. 1375–1385, Oct. 2013, doi: 10.1061/(ASCE)MT.1943-5533.0000661.

[10] F. Gong, X. Zhou, Z. You, Y. Liu, and S. Chen, "Using discrete element models to track movement of coarse aggregates during compaction of asphalt mixture," *Construction and Building Materials*, vol. 189, pp. 338–351, Nov. 2018, doi: 10.1016/j.conbuildmat.2018.08.133.

[11] G. Qian, K. Hu, J. Li, X. Bai, and N. Li, "Compaction process tracking for asphalt mixture using discrete element method," *Construction and Building Materials*, vol. 235, p. 117478, Feb. 2020, doi: 10.1016/j.conbuildmat.2019.117478.

[12] L. Wang and X. Yang, "Analysis of Optimal RAP Content Based on Discrete Element Method," *Advances in Materials Science and Engineering*, vol. 2022, pp. 1–7, Jun. 2022, doi: 10.1155/2022/2878848.

[13] C. Shi *et al.*, "Research on the evolution of aggregate skeleton characteristics of asphalt mixture under uniaxial compression loading," *Construction and Building Materials*, vol. 413, p. 134769, Jan. 2024, doi: 10.1016/j.conbuildmat.2023.134769.

[14] S. Xu, Z. Yan, L. Zhao, S. Ren, Y. Wang, and L. Chi, "A study on the mesoscopic damage of asphalt mixture under freeze-thaw cycles based on discrete element theory," *Case Studies in Construction Materials*, vol. 20, p. e02964, Jul. 2024, doi: 10.1016/j.cscm.2024.e02964.

[15] Y. Ye, Y. Sun, L. Gao, Z. Ma, and X. Xue, "Study on Creep Behavior Of Asphalt Mixture Based on Discrete Element Method," *BJRBE*, vol. 15, no. 4, pp. 174–195, Oct. 2020, doi: 10.7250/bjrbe.2020-15.500.

[16] H. Wang, W. Huang, J. Cheng, and G. Ye, "Mesoscopic creep mechanism of asphalt mixture based on discrete element method," *Construction and Building Materials*, vol. 272, p. 121932, Feb. 2021, doi: 10.1016/j.conbuildmat.2020.121932.

[17] X. Ding, T. Ma, W. Zhang, D. Zhang, and T. Yin, "Effects by property homogeneity of aggregate skeleton on creep performance of asphalt concrete," *Construction and Building Materials*, vol. 171, pp. 205–213, May 2018, doi: 10.1016/j.conbuildmat.2018.03.150.

[18] X. Ding, F. Huang, P. Rath, Z. Ye, W. G. Buttlar, and T. Ma, "Comparative fracture resistance assessment of rubber-modified asphalt mortar based on meso-and macro-mechanical analysis," *International Journal of Pavement Engineering*, vol. 24, no. 1, p. 2265032, Dec. 2023, doi: 10.1080/10298436.2023.2265032.

[19] H.-C. Dan, Z. Zhang, J.-Q. Chen, and H. Wang, "Numerical Simulation of an Indirect Tensile Test for Asphalt Mixtures Using Discrete Element Method Software," *J. Mater. Civ. Eng.*, vol. 30, no. 5, p. 04018067, May 2018, doi: 10.1061/(ASCE)MT.1943-5533.0002252.

[20] M. Chang, Z. Liu, J. Zhang, Y. Zhang, and B. Yang, "Distribution characteristics of force chains in asphalt mixtures based on indirect tensile pattern," *China Journal of Highway and Transport*, vol. 35, no. 09, pp. 224–234, Oct. 2021.

[21] Y. Peng and J. Bao, "Micromechanical Analysis of Asphalt-Mixture Shear Strength Using the Three-Dimensional Discrete Element Method," *J. Mater. Civ. Eng.*, vol. 30, no. 11, p.

04018302, Nov. 2018, doi: 10.1061/(ASCE)MT.1943-5533.0002508.

[22] D. Jelagin, E. Olsson, C. Raab, and M. N. Partl, "Experimental and numerical modelling of shear bonding between asphalt layers," *Road Materials and Pavement Design*, vol. 24, no. sup1, pp. 176–191, Apr. 2023, doi: 10.1080/14680629.2023.2180298.

[23] X. Zou, Y. Xie, Y. Bi, B. Li, W. Wang, and X. Ye, "Study on the shear strength of asphalt mixture by discrete element modeling with coarse aggregate morphology," *Construction and Building Materials*, vol. 409, p. 134058, Dec. 2023, doi: 10.1016/j.conbuildmat.2023.134058.

[24] X. Zhao, Q. Dong, X. Chen, and F. Ni, "Influence of initial defects on the fatigue behaviour of cement-stabilized macadam base through DEM," *International Journal of Pavement Engineering*, vol. 23, no. 14, pp. 4845–4856, Dec. 2022, doi: 10.1080/10298436.2021.1984473.

[25] N. H. T. Nguyen, H. H. Bui, J. Kodikara, S. Arooran, and F. Darve, "A discrete element modelling approach for fatigue damage growth in cemented materials," *International Journal of Plasticity*, vol. 112, pp. 68–88, Jan. 2019, doi: 10.1016/j.ijplas.2018.08.007.

[26] N. H. T. Nguyen, H. H. Bui, G. D. Nguyen, and J. Kodikara, "A cohesive damage-plasticity model for DEM and its application for numerical investigation of soft rock fracture properties," *International Journal of Plasticity*, vol. 98, pp. 175–196, Nov. 2017, doi: 10.1016/j.ijplas.2017.07.008.

[27] X. Li, X. Lv, X. Liu, and J. Ye, "Discrete Element Analysis of Indirect Tensile Fatigue Test of Asphalt Mixture," *Applied Sciences*, vol. 9, no. 2, p. 327, Jan. 2019, doi: 10.3390/app9020327.

[28] Y. Peng, Y. Chen, Y. Xu, S. Xia, X. Lu, and Y. Li, "Discrete element modelling of mechanical response of crumb rubber-modified asphalt pavements under traffic loads," *International Journal of Pavement Engineering*, vol. 24, no. 2, p. 2068546, Jan. 2023, doi: 10.1080/10298436.2022.2068546.

[29] Y. Peng, S. Xia, Y.-R. Xu, X.-Y. Lu, and Y.-W. Li, "Mechanical Response of Asphalt Surfaces under Moving Traffic Loads Using 3D Discrete Element Method," *J. Transp. Eng., Part B: Pavements*, vol. 148, no. 2, p. 04022006, Jun. 2022, doi: 10.1061/JPEODX.0000349.

[30] T. Ma, Y. Zhang, D. Zhang, J. Yan, and Q. Ye, "Influences by air voids on fatigue life of asphalt mixture based on discrete element method," *Construction and Building Materials*, vol. 126, pp. 785–799, Nov. 2016, doi: 10.1016/j.conbuildmat.2016.09.045.

[31] Y. Yang, L. Yue, H. Cui, and Y. Yang, "Simulation and evaluation of fatigue damage of cold recycled mixtures with bitumen emulsion," *Construction and Building Materials*, vol. 364, p. 129976, Jan. 2023, doi: 10.1016/j.conbuildmat.2022.129976.

[32] L. Gao, J. Xie, S. Jia, and Z. Zhu, "Virtual test of typeIfatigue crack of asphalt mixture based on discrete element method," *Journal of Huazhong University of Science and Technology(Natural Science Edition)*, vol. 46, no. 01, pp. 92–97, Jan. 2018.

[33] W. Feng, Y. Jian, and H. Gong, "Macro- and meso-scale experimental characterization of bending fatigue behavior evolution law for asphalt mixture," *Journal of Railway Science and Engineering*, vol. 19, no. 10, pp. 2984–2994, Oct. 2022.

[34] X. Luo, Y. Zhang, and R. L. Lytton, "Implementation of pseudo J-integral based Paris' law for fatigue cracking in asphalt mixtures and pavements," *Mater Struct*, vol. 49, no. 9, pp. 3713–3732, Sep. 2016, doi: 10.1617/s11527-015-0750-z.

[35] G. R. Irwin, "Analysis of Stresses and Strains Near the End of a Crack Traversing a Plate," *Journal of Applied Mechanics*, vol. 24, no. 3, pp. 361–364, Sep. 1957, doi: 10.1115/1.4011547.

[36] Tada H, Paris PC, and Irwin GR, *The Stress Analysis of Cracks*. Del Research Corporation, Handbook.

[37] AASHTO, *Determining the Damage Characteristic Curve and Failure Criterion Using the Asphalt Mixture Performance Tester (AMPT) Cyclic Fatigue Test. AASHTO TP 107. AASHTO, Washington DC*, Washington DC., 2018.

[38] M. L. Williams, R. F. Landel, and J. D. Ferry, "The Temperature Dependence of Relaxation Mechanisms in Amorphous Polymers and Other Glass-forming Liquids," *J. Am. Chem. Soc.*, vol. 77, no. 14, pp. 3701–3707, Jul. 1955, doi: 10.1021/ja01619a008.

[39] T. K. Pellinen, M. W. Witczak, and R. F. Bonaquist, "Asphalt Mix Master Curve Construction Using Sigmoidal Fitting Function with Non-Linear Least Squares Optimization," in *Recent Advances in Materials Characterization and Modeling of Pavement Systems*, Columbia University, New York, United States: American Society of Civil Engineers, Dec. 2003, pp. 83–101. doi: 10.1061/40709(257)6.

[40] ARA, "Guide for mechanistic-empirical design of new and rehabilitated pavement structures," Washington, DC: Transportation Research Board, 2004.

[41] Y. Zhang, B. Birgisson, and R. L. Lytton, "Weak Form Equation–Based Finite-Element Modeling of Viscoelastic Asphalt Mixtures," *J. Mater. Civ. Eng.*, vol. 28, no. 2, p. 04015115, Feb. 2016, doi: 10.1061/(ASCE)MT.1943-5533.0001395.

[42] F. Ren, "Research on viscoelastic properties and mixture performance of TB composite high modulus agent modified asphalt," *New Building Materials*, vol. 48, no. 01, pp. 98–102, 2021.

[43] Z. Zhang, Z. Tian, S. Huang, and F. Zhao, "Composition and Process Parameters of SBS-PU Modified High-Viscosity and High-Elasticity Asphalt," vol. 23, no. 01, pp. 100–107, 2020.